Journal of Colloid and Interface Science 717 (2026) 140391

Contents lists available at ScienceDirect

Journal of Colloid And Interface Science

journal homepage: www.elsevier.com/locate/jcis

Constructing MoO_2/Mo_2C heterointerfaces on N-doped carbon microspheres for synergistic adsorption-catalysis of polysulfides in Lithium-Sulfur batteries

Lin Sun [a,*], Tianqi Wang [a], Jie Xie [c,*], Yunjing Qiao [a], Xuetao Lu [a], Menghan Liu [a], Cheng Liu [d,*], Zhong Jin [b,*]

[a] School of Chemistry and Chemical Engineering, Yancheng Institute of Technology, Yancheng, 224051, China
[b] State Key Laboratory of Coordination Chemistry, MOE Key Laboratory of Mesoscopic Chemistry, MOE Key Laboratory of High Performance Polymer Materials and Technology, Jiangsu Key Laboratory of Advanced Organic Materials, Tianchang New Materials and Energy Technology Research Center, Institute of Green Chemistry and Engineering, School of Chemistry and Chemical Engineering, Nanjing University, Nanjing 210023, China
[c] Intelligent Manufacturing Institute, Yancheng Polytechnic College, Yancheng, 224005, PR China
[d] Jiangsu Key Laboratory for Chemistry of Low-Dimensional Materials, School of Chemistry and Chemical Engineering, Huaiyin Normal University, Huai'an 223001, PR China

GRAPHICAL ABSTRACT

Through the rapid and controllable construction of the MoO_2/Mo_2C heterointerface, the interfacial electronic enhancement effect is achieved, thereby balancing the adsorption-catalytic activity toward LiPSs intermediates.

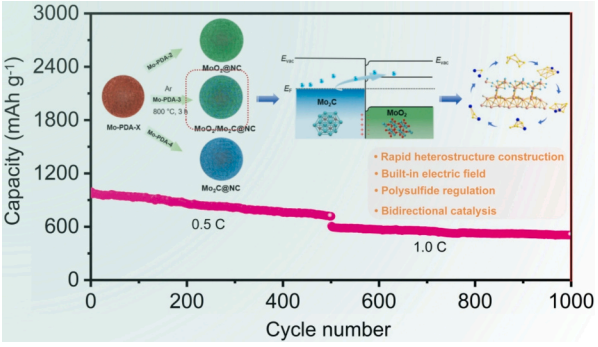

ARTICLE INFO

Keywords:
Li—S battery
MoO_2/Mo_2C
Heterostructure
Polysulfide regulation
Electrocatalyst

ABSTRACT

The practical implementation of lithium-sulfur (Li—S) batteries is severely hindered by the polysulfide shuttle effect and sluggish conversion kinetics. Herein, we designed and fabricated a heterostructured MoO_2/Mo_2C composite anchored on N-doped carbon microspheres (MoO_2/Mo_2C@NC) as a multifunctional separator coating. The built-in electric field formed at the MoO_2/Mo_2C interface drives electron redistribution, which not only strengthens the chemical anchoring of polysulfides on the polar MoO_2 surfaces but also accelerates their catalytic conversion on the conductive Mo_2C domains. This synergistic adsorption-catalysis mechanism effectively suppressed shuttle behavior and enhanced liquid-to-solid transformation kinetics. As a result, Li—S batteries equipped with the MoO_2/Mo_2C@NC-modified separator exhibited remarkable rate capability (670 mAh g^{-1} at

* Corresponding authors.
E-mail addresses: sunlin@nju.edu.cn (L. Sun), 2025170764@ycpc.edu.cn (J. Xie), 8202111024@hytc.edu.cn (C. Liu), zhongjin@nju.edu.cn (Z. Jin).

https://doi.org/10.1016/j.jcis.2026.140391
Received 15 January 2026; Received in revised form 24 March 2026; Accepted 26 March 2026
Available online 31 March 2026
0021-9797/© 2026 Elsevier Inc. All rights are reserved, including those for text and data mining, AI training, and similar technologies.

2C) and long-term cycling stability (approximately 515 mAh g^{-1} after 1000 cycles). This work elucidates the critical role of interfacial electronic modulation in polysulfide regulation and provides a rational heterostructure design strategy for high-energy-density Li—S batteries.

1. Introduction

The proliferation of portable electronics and the expansion of large-scale energy storage grids have intensified the demand for secondary battery systems with high energy density [1,2]. Among emerging energy storage technologies, lithium-sulfur (Li—S) batteries are regarded as one of the most promising candidates for next-generation high-energy-density devices because of their ultrahigh theoretical specific capacity (1675 mAh g^{-1}), high energy density (~2600 Wh kg^{-1}), and the natural abundance, low cost, and environmental benignity of sulfur [3–6]. Nevertheless, the practical deployment of Li—S batteries is still hindered by several intrinsic challenges, most notably the notorious "shuttle effect" of soluble lithium polysulfides (LiPSs) formed during the charge-discharge cycles [7–10]. This phenomenon causes irreversible loss of active materials, rapid capacity decay, low Coulombic efficiency, and severe self-discharge, which acts as a fundamental bottleneck restricting the commercialization of Li—S batteries [11–13].

Extensive research efforts have been devoted to suppressing the LiPS shuttle effect via the efficient immobilization and catalytic conversion of LiPSs [14–16]. In this context, the engineering of functional separator coatings with high-performance polar materials has emerged as an effective strategy to physically confine and chemically adsorb LiPSs [17–20]. Although carbon-based coatings were initially investigated, their non-polar character limits polysulfide affinity and confinement capability [21]. Recently, strongly polar transition metal oxides (TMOs) and transition metal carbides (TMCs) have attracted increasing interest due to their excellent adsorption and catalytic activity toward LiPSs. TMOs exhibit strong LiPS anchoring ability through M-O chemical bonds, whereas TMCs possesse metal-like electrical conductivity and high catalytic activity for LiPS conversion [22–26]. However, single-component TMA or TMC systems often suffer from a trade-off between effective LiPS adsorption and rapid conversion: the poor electrical conductivity of TMOs may impede reaction kinetics, while the LiPS adsorption strength of TMCs is insufficient relative to their catalytic performance [27,28]. These limitations prevent the optimal regulation of LiPSs and thus restrict the overall electrochemical performance of Li—S batteries.

To address this challenge, in this work, we designed and in-situ constructed a microspherical composite composed of MoO_2/Mo_2C heterostructures supported on N-doped carbon microspheres (denoted as MoO_2/Mo_2C@NC) and employed it as a multifunctional separator coating for Li—S batteries. Through a precisely controlled pyrolysis process of molybdenum and carbon precursors, we successfully fabricated nanoscale MoO_2/Mo_2C heterojunctions. Despite the significant progress achieved in heterostructure engineering for Li—S batteries, the reported heterostructured catalysts still suffer from inherent limitations that restrict their overall catalytic performance. For instance, the MoS_2/MoO_3 [29] heterostructure suffers from the poor electrical conductivity of MoO_3 and the insufficient catalytic activity of MoS_2, which leads to sluggish LiPS conversion kinetics. The MoS_2/TiO_2 [30] system is plagued by weak interfacial coupling induced by lattice mismatch, which impedes efficient charge transfer and thus results in only moderate LiPS adsorption capability. Although the Mo_2C/MoC [31] heterostructure exibits enhanced electrical conductivity, the relatively weak polarity of both carbide components results in unsatisfactory chemical anchoring of LiPSs. Compared with previously reported heterostructured systems, the MoO_2/Mo_2C heterojunction proposed in this work possesses distinct design advantages. First, the significant work function difference between MoO_2 and Mo_2C promotes the formation of a strong built-in electric field, which drives interfacial charge redistribution and simultaneously enhances the LiPS adsorption capability of MoO_2 and the catalytic activity of Mo_2C. Second, the MoO_2/Mo_2C heterostructure directly couples the highly adsorptive MoO_2 with the highly conductive Mo_2C at the nanoscale, enabling the captured LiPSs to migrate rapidly across a low-resistance interface to the catalytic active sites, thus achieving a short-path "adsorption-conversion" synergy. Third, theoretical calculations demonstrate that the MoO_2/Mo_2C heterojunction can modulate the d-band center of Mo to be closer to the Fermi level, which systematically reduces the energy barriers of the multi-step LiPS conversion reactions. Fourth, the simultaneously introduced nitrogen-doped carbon (NC) support further improves the dispersion of MoO_2/Mo_2C heterostructures and facilitates electron transport throughout the composite. Electrochemical tests confirmed that, in comparison with single-component MoO_2@NC or Mo_2C@NC coatings, Li—S cells with the MoO_2/Mo_2C@NC-modified separator exhibited significant improvements in both rate capability and long-term cycling stability. Therefore, the rationally designed MoO_2/Mo_2C@NC heterojunction, via precise interfacial electronic engineering and structural design, provides a novel strategy for the synergistic enhancement of LiPS anchoring and conversion of in Li—S batteries.

2. Experimental section

2.1. Materials

All chemical reagents were purchased commercially and used without further purification unless otherwise stated. Ammonium molybdate tetrahydrate ($(NH_4)_6Mo_7O_{24}{\cdot}4H_2O$, analytical grade) and anhydrous ethanol were purchased from Shanghai Titan Scientific Co., Ltd. Dopamine hydrochloride ($C_8H_{12}ClNO_2$, analytical grade) and tris (hydroxymethyl)aminomethane ($C_4H_{11}NO_3$, analytical grade) were obtained from Xiya Chemical Technology (Shandong) Co., Ltd. Sulfur (S, analytical grade) and lithium sulfide (Li_2S, analytical grade) were supplied by Aladdin Reagent (Shanghai) Co., Ltd. Carbon nanotubes (CNTs) were provided by Nanjing XFNANO Materials Tech Co., Ltd. Battery-grade high-purity solvents and electrolytes were sourced from Dodo-Chem. Deionized water was used in all experimental procedure.

2.2. Synthesis of MoO_2/Mo_2C@NC heterostructures

The MoO_2/Mo_2C@NC heterostructures were synthesized as follows. First, 0.1 g of $(NH_4)_6Mo_7O_{24}{\cdot}4H_2O$ and 0.3 g of $C_8H_{12}ClNO_2$ with a mass ratio 1:3 were dissolved in 50 mL of $C_4H_{11}NO_3$ Tris buffer solution (10 mM, pH = 8.5). After continuous magnetic stirring overnight, the resulting precursor precipitate was collected by centrifugation, washed thoroughly with deionized water and ethanol, and then dried at 70 °C under vacuum. The as-obtained precursor was subsequently annealed at 800 °C for 3 h under an argon atmosphere with a heating rate of 5 °C·min^{-1} to prepare MoO_2/Mo_2C@NC microspheres. For comparison, pure MoO_2@NC and Mo_2C@NC samples were also prepared via the same method by adjusting the mass ratios of $(NH_4)_6Mo_7O_{24}{\cdot}4H_2O$ to $C_8H_{12}ClNO_2$ to 1:2 and 1:4, respectively. In addition, we also physically mixed the as-prepared MoO_2@NC and Mo_2C@NC samples in the same molar ratio of MoO_2 to Mo_2C as in the MoO_2/Mo_2C@NC sample to obtain a control sample, which was denoted as MoO_2/Mo_2C-mix.

2.3. Material characterizations

The crystal phase structure of the samples were characterized by X-ray diffraction (XRD, X'Pert3Powder, PANalytical, Netherlands) with

Cu-Kα radiation. The morphological features of the prepared samples were characterized by Scanning electron microscopy (SEM, FEI Nova NanoSEM 450) and high-resolution of transmission electron microscopy (HRTEM, JEM-2100F). Energy Dispersive X-ray spectroscopy (EDS) and elemental mapping were performed on an X-MaxN 80 T IE250 spectrometer (Oxford company, UK). Raman spectra were recorded on a Raman Microscope (HORIBA Scientific LabRAM HR Evolution) with a 532 nm laser excitation. The surface chemical composition and valence states of the obtained samples was analyzed by X-ray photoelectron spectroscopy (XPS, Thermo Fisher Scientific, ESCALAB 250Xi). The XPS binding energy was calibrated with the C 1 s peak at 284.8 eV as the reference. The sulfur content in the cathodes and the carbon content in the prepared samples were quantified by the thermogravimetric analysis (TGA, STA499f5 analyzer) with heating rate of 10 °C min^{-1}. UV–visible (UV–vis) absorption spectra were recorded on a UV-1800PC spectrophotometer (Shanghai Mapada Instruments Co., Ltd.) The electrolyte wettability of the pristine PP and modified PP separators was evaluated by contact angle measurements on a contact angle analyzer (JKRUSS DSA100).

2.4. Fabrication of modified separator and Sulfur cathode

A MoO_2/Mo_2C@NC-modified separator was fabricated via a simple blade-coating process. Specifically, a homogeneous slurry was prepared by mixing 70 wt% MoO_2/Mo_2C@NC, 20 wt% carbon nanotubes (CNTs), and 10 wt% polyvinylidene fluoride (PVDF) in *N*-methyl-2-pyrrolidone (NMP) under vigorous stirring. The prepared slurry was then uniformly coated onto the surface of a pristine Celgard 2500 polypropylene (PP) separator. The coated separator was then punched into circular discs with a diameter of 19 mm. The areal mass loading of the MoO_2/Mo_2C@NC interlayer was approximately 0.3 mg·cm^{-2}.

The sulfur-carbon nanotube (CNT/S) composite was prepared via a melt-diffusion method. Briefly, CNTs and sulfur powder were thoroughly ground together at a mass ratio of 1:4 and heated at 155 °C for 10 h. The sulfur areal loading on the prepared electrode was about 2 mg cm^{-2}.

2.5. Preparation of Lithium polysulfide (Li_2S_6) solution and adsorption tests

A Li_2S_6 solution was prepared by dissolving S and Li_2S at a molar ratio of 5:1 in a mixed solvent of 1,2-dimethoxyethane (DME) and 1,3-dioxolane (DOL) (*v*/v = 1:1). The solution was stirred vigorously at 65 °C for 12 h. For the adsorption test, 10 mg of the sample was introduced into 3 mL of 5 mM Li_2S_6 solution. After immersing the sample in the Li_2S_6 solution for 12 h, ultraviolet-visible (UV–vis) absorption spectra were recorded. All the above procedures were carried out in an argon-filled glove box to maintain an inert atmosphere.

2.6. Symmetric cell assembly and evaluation of polysulfide conversion kinetics

The active material and PVDF were mixed at a mass ratio of 9:1 in NMP solvent to form a homogeneous slurry, which was then coated onto an aluminum (Al) foil current collector. A 0.5 M Li_2S_6 electrolyte was prepared by dissolving S and Li_2S in a solvent mixture of DOL and DME (*v*/v = 1:1) containing 1 M LiTFSI, followed by stirring at 65 °C overnight in an argon-filled glove box. For electrochemical tests, symmetric cells were assembled using two identical electrodes as the working and counter electrodes, each with an active material mass loading of 1.0 mg cm^{-2}. Each cell was filled with 25 μL of 0.5 M Li_2S_6 electrolyte. Cyclic voltammetry (CV) measurements were performed within a voltage window of −1.0 to 1.0 V. Electrochemical impedance spectroscopy (EIS) was carried out over a frequency range of 0.01 to 10^5 Hz.

2.7. Li_2S nucleation and dissolution experiments

To investigate the liquid-solid conversion kinetics, a 0.2 M Li_2S_8 solution was prepared by mixing S and Li_2S at a molar ratio of 7:1 in tetraethylene glycol dimethyl ether (TEGDME), followed by vigorous stirring. The deposition of Li_2S on different substrates was studied using CR2025 coin cells with Celgard 2500 PP separators. In these experiments, the cathode side was loaded with 25 μL of 0.5 M Li_2S_8 solution, and 25 μL of LiTFSI electrolyte was added to the anode side. The cells were discharged galvanostatically at 0.1 mA to 2.06 V, followed by a potentiostatic hold at 2.05 V until the current dropped below 10^{-5} A to facilitate Li_2S nucleation. The Li_2S nucleation capacity was determined by integrating the corresponding current-time curve based on Faraday's law.

Following the Li_2S deposition tests, the same cells were charged galvanostatically at 0.1 mA to 1.7 V to ensure complete Li_2S nucleation, followed by a potentiostatic charge at 2.4 V until the current decreased below 10^{-5} A to promote Li_2S dissolution. The Li_2S dissolution capacity was calculated by integrating the current–time profile according to Faraday's law.

2.8. Li—S battery assembly and electrochemical performance evaluation

The cathode was fabricated by mixing the CNT/S composite, Super P, and PVDF at a weight ratio of 8:1:1 in NMP to form a homogeneous slurry. This slurry was coated onto Al foil, vacuum-dried at 45 °C overnight, and then cut into 12 mm diameter discs. The resulting S electrodes exhibited a S mass loading of approximately 1 mg cm^{-2}. CR2025 coin-type half-cells were assembled in an argon-filled glove box (with oxygen and moisture levels maintained below 0.1 ppm) using Li metal as the counter/reference electrode and Celgard 2500 PP as the separator. The electrolyte consisted of 1.0 M lithium bis(trifluoromethanesulfonyl)imide (LiTFSI) in a mixture of DOL and DME (*v*/v = 1:1) with 1 wt% $LiNO_3$ as an additive. Galvanostatic charge/discharge measurements were performed using a LAND CT2001A battery test system (China) within a voltage window of 1.7–2.8 V at various current rates (1C = 1675 mA g^{-1}, based on the S mass). CV and EIS were conducted on a CHI660E electrochemical workstation (Chenhua, China). EIS measurements were carried out over a frequency range of 0.01 Hz to 10^5 Hz. All electrochemical tests were performed at 28 °C. The specific capacities of the Li—S batteries were calculated based on the mass of S in the cathode.

2.9. Theoretical calculation methods

Density functional theory (DFT) calculations were carried out using the Cambridge sequential total energy package (CASTEP) module of Materials Studio software for evaluating the electrochemical performance of MoO_2, Mo_2C and MoO_2/Mo_2C. The generalized gradient approximation in the Perdew–Burke–Ernzerhof pseudopotentials (GGA-PBE) was used to model the exchange–correlation effects. A plane-wave cutoff energy of 450 eV was applied. Before energy calculations, all atomic models underwent geometric optimization with the following convergent tolerances: the changes of energy, the maximum stress and the maximum displacement were 2×10^{-5} eV $atom^{-1}$, 0.1 GPa and 0.002 Å, respectively. For the three catalysts (MoO_2, Mo_2C, and MoO_2/Mo_2C), all slab models were constructed based on their optimized bulk structures. The bulk MoO_2 structure was adopted from the experimental crystal data (JCPDS No. 78–1069) with a monoclinic phase (space group P21/c). The exposed facet was selected as the (110) plane, which is the most thermodynamically stable and commonly exposed surface in practical applications. Meanwhile, the bulk Mo_2C structure was a hexagonal phase (space group $P6_3/mmc$, JCPDS No. 35–0787), and the (101) facet was chosen as the exposed surface. The typical LiPSs species involved in the Li—S battery reaction process were selected for calculation, including Li_2S_8, Li_2S_6, Li_2S_4, Li_2S_2, and Li_2S. All LiPSs molecules

were optimized in the gas phase first to obtain their stable configurations, and then adsorbed on the catalyst surfaces for subsequent calculations. To avoid artificial interactions caused by periodicity between adjacent layers in adsorption models, the pristine MoO_2, Mo_2C and MoO_2/Mo_2C models are set with 10 Å. The PBE + U functionals (with parameters of U = 3.0 eV) were chosen for calculating the density of states, which expands the valence electrons states in a plane-wave basis set.

3. Results and discussion

The MoO_2/Mo_2C@NC composite was synthesized via a facile solution method combined with a subsequent pyrolysis process. As illustrated in Fig. 1a, polydopamine (PDA) was chosen as the carbon and nitrogen precursor due to its abundant catechol and amino groups that can chelate and adsorb Mo^{6+} ions during self-polymerization. $(NH_4)_6Mo_7O_{24}{\cdot}4H_2O$ and $C_8H_{12}ClNO_2$ were mixed at a mass ratio of 1:3 in a 10 mM Tris-buffer solution. The collected precursor precipitate after centrifugation and washing was subjected to high-temperature pyrolysis under an argon atmosphere to form MoO_2/Mo_2C@NC microspheres. Notably, pure MoO_2@NC and Mo_2C@NC samples were successfully prepared by simply adjusting the mass ratio of DA·HCl to the molybdate precursor to 1:2 and 1:4, respectively. The as-prepared MoO_2/Mo_2C@NC composite exhibits a uniform micron-sized spherical morphology (**Fig. S1b**, **Figs. S1a-b**). Further TEM characterization demonstrates that the microspheres are assembled from numerous hierarchical nanosheets (Fig. 1c and **Figs. S1c**, **d**). The reference Mo_2C@NC and MoO_2@NC samples also present similar microsphere morphological features (**Figs. S2**, **S3**), indicating that materials with distinct compositions but analogous architectures can be conveniently synthesized by adjusting the DA·HCl/molybdenum salt mass ratio, which provides convenience for subsequent comparative studies.

Fig. 1d shows a HRTEM image of the MoO_2/Mo_2C@NC sample, where clear lattice fringes with d-spacings of 0.23 nm and 0.34 nm are observed, corresponding to the (101) plane of hexagonal Mo_2C and the (011) plane of monoclinic MoO_2, respectively [32–34].A distinct heterointerfacial boundary between the two phases is clearly resolved, providing direct experimental evidence for the successful formation of the MoO_2/Mo_2C heterojunction. Elemental mapping analysis of MoO_2/Mo_2C@NC (Figs. 1e-j) further demonstrates the homogeneous distribution of Mo, O, and N elements throughout the microspheres, while the strong C signal originates from the N-doped carbon matrix serving as the support. This result confirms the successful construction of the N-doped carbon framework in the obtained composite.

Thermogravimetric analysis (TGA) was performed to accurately quantify the carbon content in the synthesized samples (**Fig. S4**), and the carbon contents of MoO_2/Mo_2C@NC, Mo_2C@NC, and MoO_2@NC were determined to be 37.4%, 31.6%, and 41.0%, respectively. Notably, Mo_2C@NC had the lowest carbon content and MoO_2@NC the highest, a trend consistent with the proposed reaction mechanism: carbon derived from carbonized PDA partially reacts with in-situ formed MoO_2 (from molybdate precursor decomposition) at high temperature to generate Mo_2C. The reaction can be expressed as follows:

$$3(NH_4)_6Mo_7O_{24} \xrightarrow{\Delta} 21MoO_2 + 4NH_3 + 14N_2 + 30H_2O$$

$$2MoO_2 + 5C \rightarrow Mo_2C + 4CO$$

The coating thickness of the MoO_2/Mo_2C@NC on the PP separator

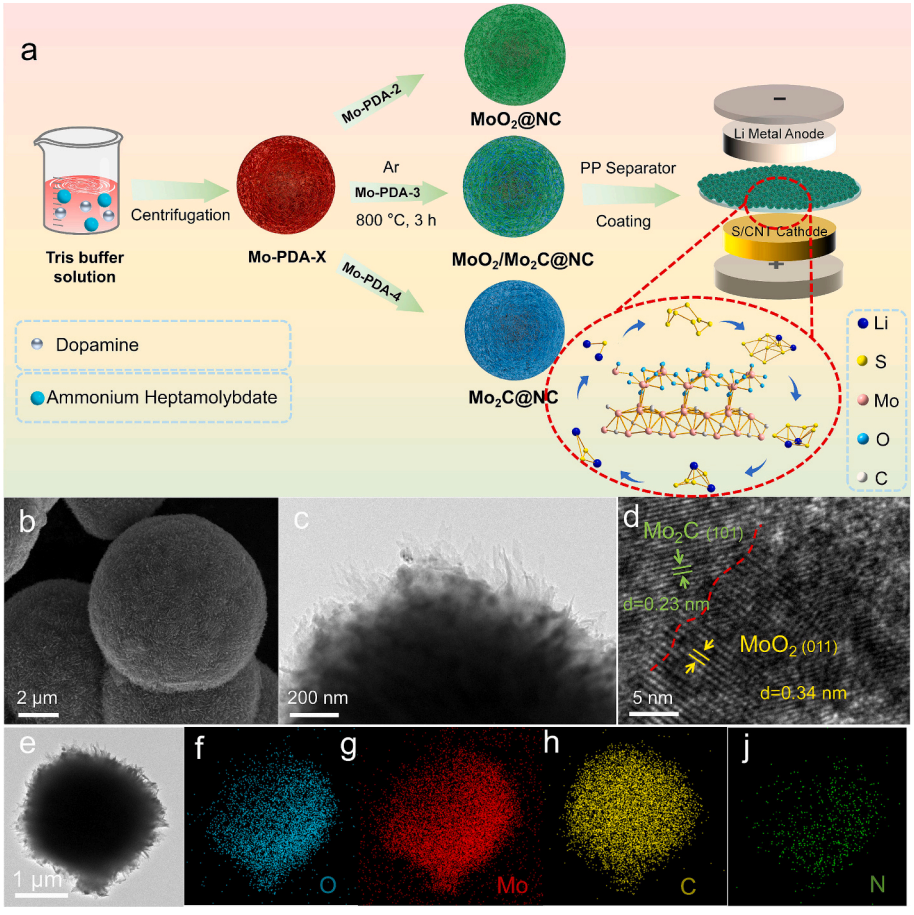

Fig. 1. (a) Schematic diagram of the preparation process of the MoO_2/Mo_2C@NC heterojunction catalyst; (b) SEM image of MoO_2/Mo_2C@NC; (c) TEM and (d) HRTEM images of MoO_2/Mo_2C@NC; (e-i) TEM image and the corresponding elemental distribution of MoO_2/Mo_2C@NC.

was approximately 6 μm (**Fig. S5**). The thermal stability of the pristine and modified separators was evaluated by isothermal heating at 30 °C and 120 °C for 0.5 h (Fig. 2**a** and **b**). At 30 °C, both separators maintained their original shape without obvious deformation. However, after heating at 120 °C, the pristine PP separator underwent severe shrinkage and structural collapse, while the MoO_2/Mo_2C@NC/PP-coated PP separator retained its structural integrity. This excellent thermal stability is attributed to the robust MoO_2/Mo_2C@NC framework that restrains the thermal motion of PP molecular chains, confirming the enhanced thermal safety of the composite separator for high performance Li—S batteries.

Fig. 2c shows the XRD patterns of MoO_2/Mo_2C@NC, Mo_2C@NC, and MoO_2@NC. For Mo_2C@NC, For Mo_2C@NC, the characteristic diffraction peaks at ~34.4°, 37.9°, and 39.4° correspond to the (100), (002), and (101) planes of hexagonal Mo_2C (JCPDS No. 35–07875) [35]. For MoO_2@NC, the peaks at ~26.0°, 37.2°, and 53.5° are assigned to the (011), (002), and (220) planes of monoclinic MoO_2 (JCPDS No. 78–1069) [36]. The XRD pattern of MoO_2/Mo_2C@NC contains all characteristic peaks of both Mo_2C and MoO_2 without any impurity peaks, confirming the coexistence of the two phases. Raman spectroscopy was used to further characterize the structural features of the samples (Fig. 2d). All samples exhibit the D band (~1359 cm^{-1}) and G band (~1590 cm^{-1}) of N-doped carbon, with I_D/I_G ratios of 1.13, 1.39, and 1.10 for MoO_2/Mo_2C@NC, Mo_2C@NC, and MoO_2@NC, respectively, indicating a higher graphitization degree of carbon in MoO_2/Mo_2C@NC and MoO_2@NC after high temperature treatment. Mo_2C@NC shows characteristic Raman peaks at ~145, 200, and 300 cm^{-1} corresponding to Mo_2C vibration modes [37], while MoO_2@NC displays peaks at ~280, 380, and 820 cm^{-1} attributed to MoO_2 [38]. The Raman spectrum of MoO_2/Mo_2C@NC retains all characteristic peaks of Mo_2C and MoO_2 with slight blue shifts, suggesting interfacial interactions between the two phases. In contrast, the physically mixed MoO_2/Mo_2C-mix sample shows no obvious peak shifts, confirming that the blue shifts in MoO_2/Mo_2C@NC originate from strong interfacial coupling and charge transfer rather than particle size effects or carbon matrix dispersion.

X-ray photoelectron spectroscopy (XPS) was employed to analyze the chemical composition and valence states of the samples (**Fig. S6**). The survey spectra confirm the presence of only Mo, O, C and N elements with no detectable impurities, and the C 1 s peak shows no obvious shift due to the weak impact of heterojunction electron transfer on the carbon support (**Fig. S7**). The high-resolution Mo 3d spectrum of MoO_2/Mo_2C@NC (Fig. 2e) can be deconvoluted into three doublets: 232.4 eV/234.6 eV for Mo^{4+} $3d_{5/2}/3d_{3/2}$ in MoO_2, 229.7/232.9 eV for Mo in Mo_2C, and 232.8 eV/236 eV for another Mo^{4+} species in MoO_2 [39,40]. Notably, the Mo 3d binding energies in MoO_2/Mo_2C@NC shift to lower values compared with MoO_2@NC, and to higher values relative to Mo_2C@NC. The high-resolution O 1 s spectra (Fig. 2f) further confirms electron transfer from Mo_2C to MoO_2 upon heterojunction formation, leading to the establishment of an internal electric field directed from

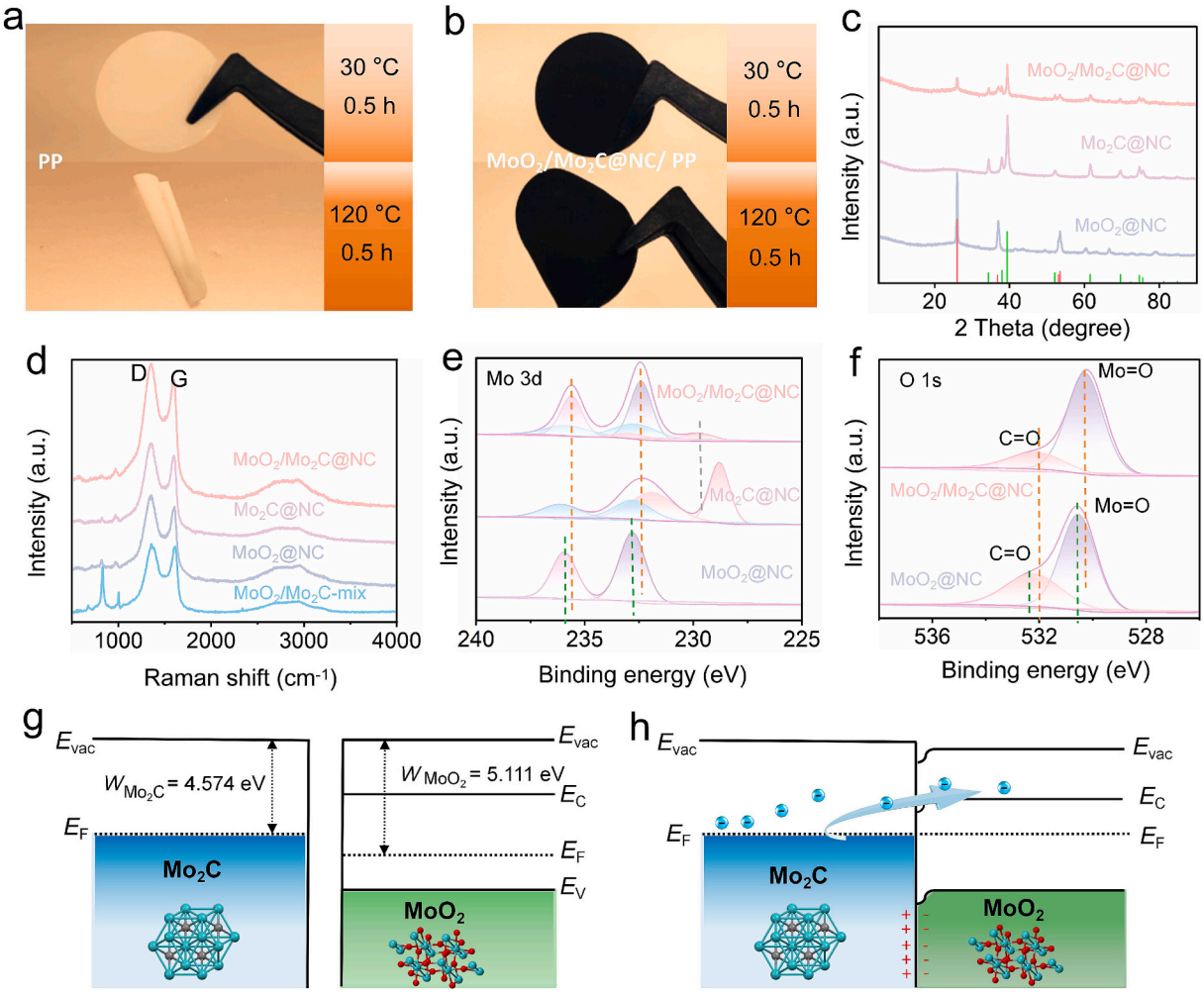

Fig. 2. Thermal stability of (a) PP and (b) MoO_2/Mo_2C@NC/ PP separators; (c) XRD patterns of MoO_2/Mo_2C@NC, Mo_2C@NC, and MoO@NC; (d) Raman spectra of MoO_2/Mo_2C@NC, Mo_2C@NC, MoO_2@NC and MoO_2/Mo_2C-mix; XPS spectra of MoO_2/Mo_2C@NC: (e) Mo 3d spectrum and (f) O 1 s spectrum. Schematic diagrams of band structure for Mo_2C and MoO_2 (g) before and (h) after formation of heterogeneous interfaces.

Mo_2C to MoO_2 [41,42].

The electronic structure modulation induced by the MoO_2/Mo_2C heterointerface was elucidated by work function calculations (Fig. 2g, h, **Fig. S8**). The work functions of pristine Mo_2C and MoO_2 were calculated to be 4.574 eV and 5.111 eV, respectively. When the MoO_2/Mo_2C heterojunction forms, electrons transfer from the lower-work-function Mo_2C to the higher-work-function MoO_2 until the Fermi levels reach equilibrium [43]. This interfacial charge redistribution induces a strong built-in electric field, which accelerates charge transport and modulates the surface adsorption energy and conversion kinetics of LiPSs, thus enhancing the overall electrochemical performance of Li—S batteries [44].

The LiPS trapping capability of the catalysts was evaluated by static adsorption tests in 5 mM Li_2S_6 solution (Fig. 3a). The Li_2S_6 solution containing MoO_2/Mo_2C@NC was nearly completely decolorized, and the UV–visible (UV–vis) absorption spectrum further confirms the strongest adsorption capability of MoO_2/Mo_2C@NC, followed by MoO_2@NC, Mo_2C@NC and the blank sample. This result indicates that the MoO_2/Mo_2C heterointerface effectively enhances Li_2S_6 adsorption, while a balance between LiPS adsorption and conversion is still critical for optimal electrochemical performance [45].

The electrolyte wettability of the pristine PP separator and the MoO_2/Mo_2C@NC-modified PP separator was examined through contact angle measurements (Figs. 3b and **3c**). The pristine PP separator shows a large contact angle of ~36.6° due to its hydrophobic nature, while the MoO_2/Mo_2C-modified separator exhibits a sharply reduced contact angle of ~22.9°, with rapid electrolyte spreading. This improved wettability originates from the polar MoO_2/Mo_2C@NC coating, which enhances the electrolyte affinity and facilitates the formation of a continuous ion-conducting network. Cyclic voltammetry (CV) tests of Li_2S_6 symmetric cells were conducted to probe the catalytic activity toward LiPS redox reactions (Fig. 3d). The blank cell displays a negligible current response, indicating sluggish LiPS conversion. Cells with Mo_2C@NC or MoO_2@NC show only weak redox peaks, while the cell with MoO_2/Mo_2C@NC exhibits pronounced and well-defined current peaks corresponding to the reduction of S_6^{2-} to lower-order LiPSs and their re-oxidation, confirming that the MoO_2/Mo_2C heterointerface significantly accelerates LiPS conversion kinetics.

The discharge/charge voltage profiles of Li—S batteries with different separators at 0.1C are compared in Fig. 3e. The battery with the MoO_2/Mo_2C@NC-modified separator shows a smaller capacity contribution from the high-voltage plateau (Q_H, S_8 to Li_2S_4) and a larger capacity from the low-voltage plateau (Q_L, Li_2S_4 to Li_2S_2/Li_2S), accompanied by a reduced voltage gap ($\Delta E \sim 0.1$ V) between charge and

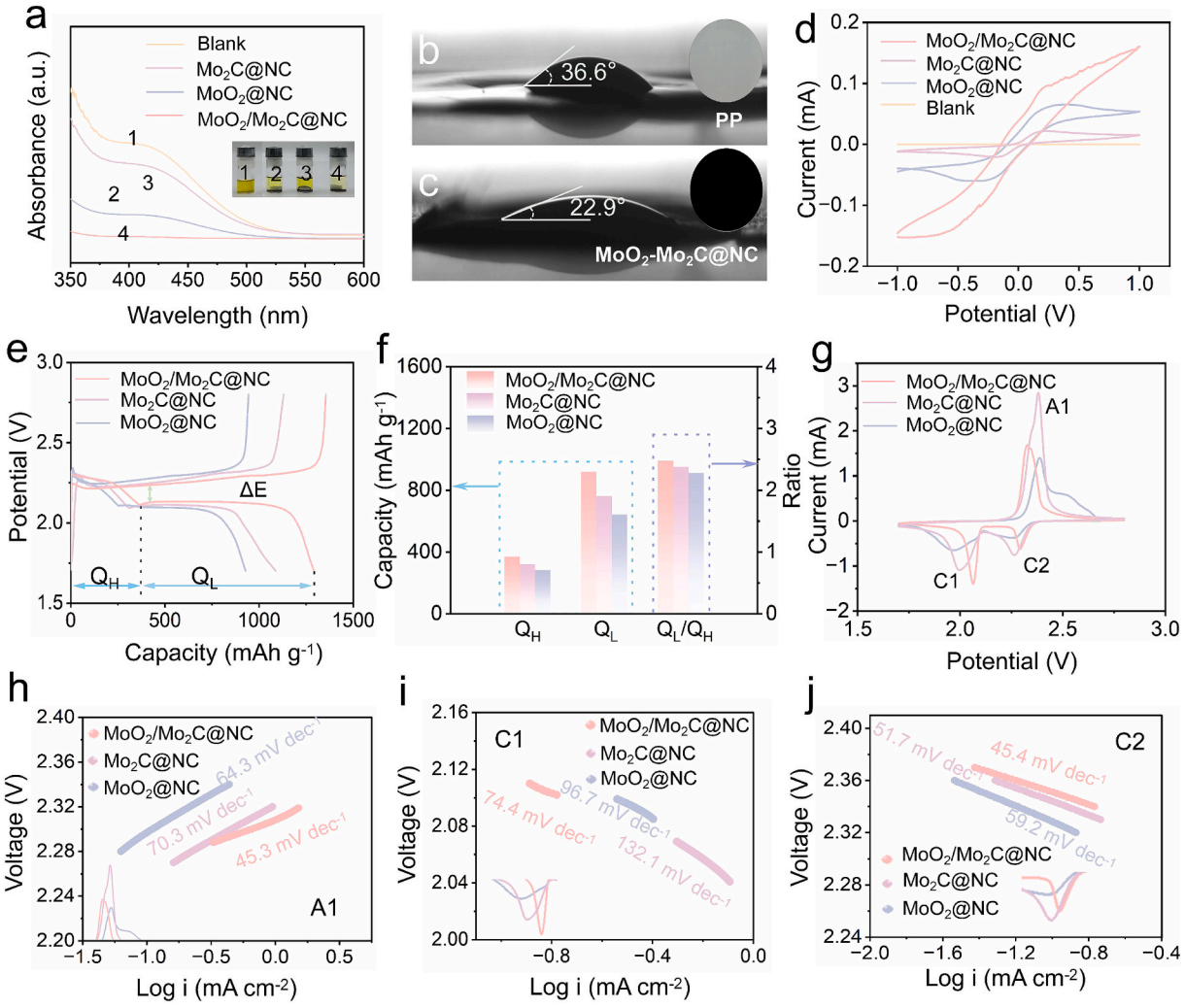

Fig. 3. (a) UV–Vis spectra of Li_2S_6 solution with blank and different catalysts (inset shows the corresponding digital photos); The contact angle of electrolyte droplets on (b) PP and (c) MoO_2/Mo_2C@NC modified PP separator; (d) CV curves of Li_2S_6 symmetric cells based on different separators at a sweep rate of 2 mV s^{-1}; (e) Comparison of voltage profiles of Li—S batteries based on various separators at 0.1C; (f) The corresponding summaries of ΔE(V) and Q_L/Q_H ratio at 0.1C; (g) The CV curves of Li—S batteries equipped with different separators under the scan rate of 0.2 mV s^{-1} within a voltage window of 1.7–2.8 V; The fitting Tafel slopes based on (h) A1, (i) C1, and (j) C2, respectively.

discharge plateaus compared with batteries with MoO_2@NC or Mo_2C@NC. The quantitative summary (Fig. 3f) reveals that the MoO_2/Mo_2C@NC-based cell has the largest Q_L/Q_H ratio (~2.48), indicating stronger catalytic conversion capability toward S_8 molecules and efficient liquid-to-solid LiPS transformation.

CV curves of Li—S batteries with different separators at a scan rate of 0.2 mV s^{-1} are shown in Fig. 3g (first three cycles in **Fig. S9**), with two reduction peaks (C1: S_8 → Li_2S_4; C2: Li_2S_4 → Li_2S_2/Li_2S) and one oxidation peak (A1: Li_2S_2/Li_2S → S_8) corresponding to typical LiPS redox processes. For the MoO_2/Mo_2C@NC-based cell, the C1 and C2 peaks shift to higher potentials while the A1 peak shifts to a lower potential (**Fig. S10**), indicating reduced reaction energy barriers. The significantly enhanced peak are consistent with the symmetric cell results, confirming accelerated electrochemical kinetics. Tafel slopes were derived to quantify the redox reaction kinetics (Figs. 3h-j). The MoO_2/Mo_2C@NC-based cell exhibits the smallest Tafel slope for A1 (45.3 mV dec^{-1}), C1 (74.4 mV dec^{-1}) and C2 (45.4 mV dec^{-1}) compared with Mo_2C@NC and MoO_2@NC, confirming that the heterointerfacial structure accelerates all key LiPS redox steps, including Li_2S oxidation, S_8 reduction and deep LiPS reduction to Li_2S.

To investigate diffusion-dominated electrochemical kinetics, CV tests were performed at scan rates from 0.1 to 0.5 mV s^{-1} (Figs. 4a-c). All samples show peak potentials shifts with increasing scan rates: reduction peaks (C1, C2) move to lower potentials and the oxidation peak (A1) to higher potentials, a typical polarization effect of diffusion-controlled reactions [46]. Notably, the cell with MoO_2/Mo_2C@NC displays the sharpest peaks and the smallest potential shifts at high scan rates, indicating superior kinetic stability attributed to the catalytic effect of the heterointerface on LiPS conversion [47]. The linear relationship between peak current and the square root of scan rate (Figs. 4d-f) follows the Randles-Sevcik equation, enabling quantitative analysis of ion diffusion kinetics. MoO_2/Mo_2C@NC exhibits the steepest slope for A1, C1 and C2, confirming that the heterointerfacial structure accelerates Li^+ and LiPS diffusion during all redox processes.

Li_2S nucleation and dissolution behaviors were evaluated by chronoamperometry to further probe liquid-solid conversion kinetics. The MoO_2/Mo_2C@NC-modified separator exhibits a higher nucleation current and a significantly larger total Li_2S deposition capacity compared with Mo_2C@NC and MoO_2@NC (Fig. 4g-i), indicating that the MoO_2/Mo_2C interface provides abundant nucleation sites and lowers the energy barrier for Li_2S formation, thus suppressing the growth of large Li_2S particles. Complementary Li_2S dissolution tests (**Figs. S11a-c**) show that the MoO_2/Mo_2C@NC-based system has the highest dissolution current and capacity, confirming that the heterogeneous structure not only

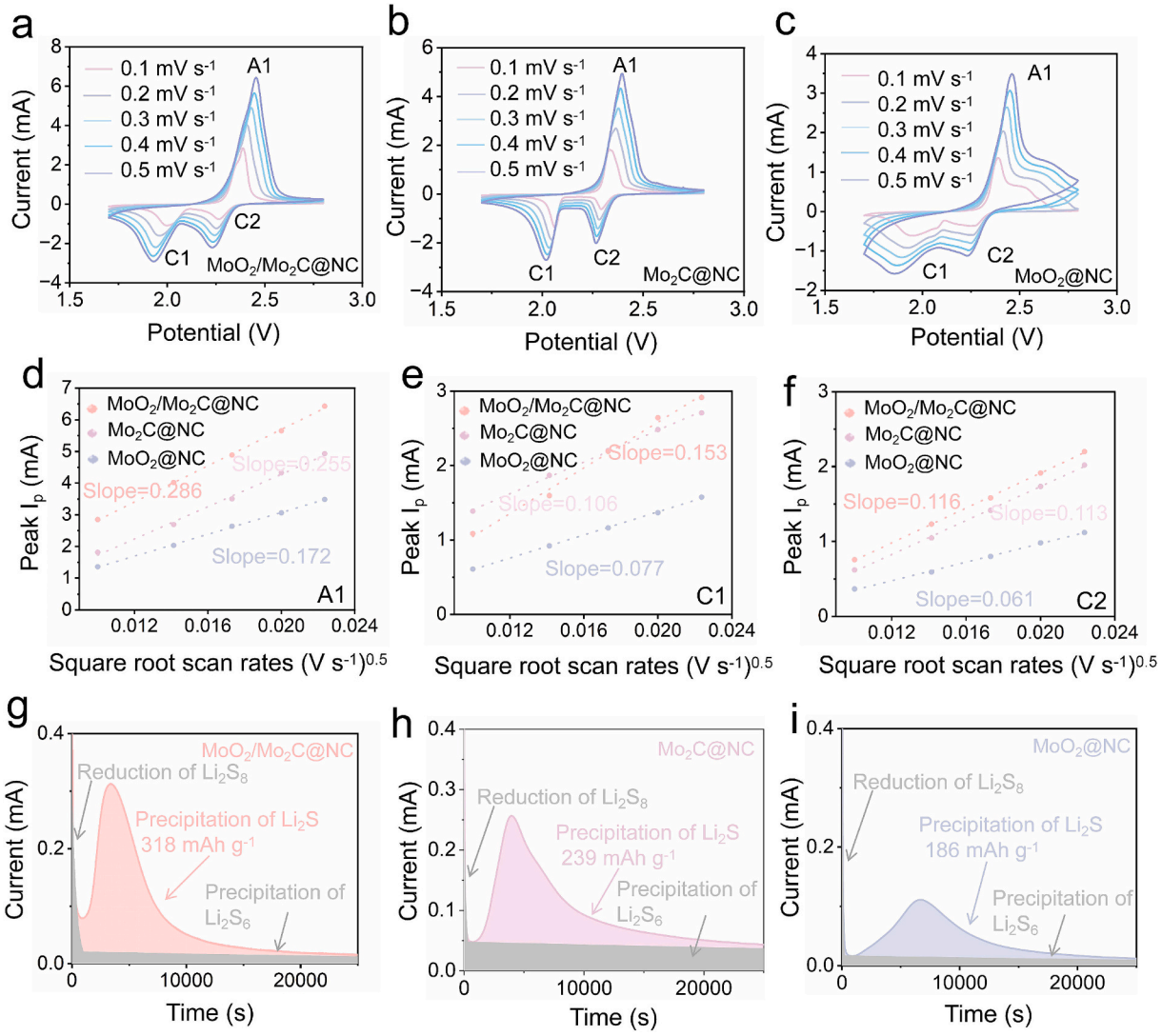

Fig. 4. CV curves of Li—S batteries based on PP separator modified with (a) MoO_2/Mo_2C@NC, (b) Mo_2C@NC, (c) MoO_2@NC at various scan rates; Plots of peak currents for (d) A1, (e) C1, and (f) C2 versus the square roots of their corresponding scan rates; Li_2S nucleation test using different modified PP separators: (g) MoO_2/Mo_2C@NC, (h) Mo_2C@NC, (i) MoO_2@NC, respectively.

facilitates Li_2S nucleation but also promotes its reversible dissolution during charging, leading to high material utilization of active material and enhanced long-term cycling stability.

Density functional theory (DFT) calculations with PBE + U functional (U = 3.0 eV for Mo 3d) were performed to investigate the electronic structure and LiPS adsorption properties of the catalysts. The differential charge density of the MoO_2/Mo_2C heterostructure (Fig. 5a) shows distinct charge accumulation (purple) on MoO_2 and charge depletion (yellow) on Mo_2C at the heterointerface, confirming electron transfer from Mo_2C to MoO_2, which is consistent with the work function analysis. Statistical analysis along the *Z*-axis (Fig. 5b) quantifies the localized charge polarization near the interface, which enhances the electrostatic interaction between the heterostructure and polar LiPSs.

The adsorption energies of typical LiPS species (Li_2S_8, Li_2S_6, Li_2S_4, Li_2S_2, Li_2S) on MoO_2/Mo_2C, Mo_2C/MoO_2, Mo_2C and MoO_2 surfaces were calculated (Fig. 5c, **Figs. S12**, **S13**). For all LiPSs, the adsorption energies on the heterostructure catalysts are more negative than those on single-component Mo_2C or MoO_2, demonstrating that the MoO_2/Mo_2C heterojunction enhances LiPS chemisorption, which is critical for suppressing the LiPS shuttle effect. The Gibbs free energy changes for the stepwise reduction of S_8 to Li_2S were calculated to probe the catalytic effect of the heterostructure (Fig. 5d). MoO_2/Mo_2C exhibits the smallest free energy change for each reaction step compared with single-component Mo_2C, MoO_2 and Mo_2C/MoO_2, confirming that the heterostructure reduces the reaction energy barrier for deep LiPS reduction and promotes the conversion of soluble LiPSs to insoluble Li_2S, with MoO_2 dominating LiPS adsorption and Mo_2C accelerating catalytic conversion [48].

Partial density of states (PDOS) analysis was performed to elucidate the electronic structure modulation of the heterostructure (Fig. 5e, **Fig. S14**). The d-band center of Mo in MoO_2/Mo_2C is closer to the Fermi level compared with single-component Mo_2C and MoO_2. A d-band center near the Fermi level strengthens the interaction between the catalyst and reaction intermediates, facilitating both intermediate adsorption and product desorption, which explains the superior catalytic performance of MoO_2/Mo_2C in LiPS conversion.

The electrochemical performance of Li—S batteries with MoO_2/Mo_2C@NC, Mo_2C@NC and MoO_2@NC-modified separators was systematically evaluated (Fig. 6). Fig. 6a presents the long-term cycling stability tests of cells equipped with these modified separators, using CNT/S cathodes with a sulfur loading of 80% (**Fig. S15**). Under conditions of a sulfur areal loading of 2 mg cm^{-2} and an E/S ratio of 7 μL mg^{-1}, the cells were cycled 1000 times (500 cycles at 0.5C followed by 500 cycles at 1.0C). The MoO_2/Mo_2C@NC modified separator exhibits the highest reversible specific capacity and remarkable cycling stability, maintaining ~515 mAh g^{-1} after 1000 cycles. In contrast, batteries with Mo_2C@NC, MoO_2@NC and MoO_2/Mo_2C-mix-modified separators show more significant capacity decay with much lower retained capacities (**Fig. S16**). Electrochemical impedance spectroscopy (EIS) results (**Fig. S17**) confirm that MoO_2/Mo_2C@NC has the smallest charge transfer resistance before cycling, attributed to its optimized interfacial compatibility and efficient ion/electron transport.

The rate capability of the batteries was tested at current densities from 0.1C to 2C (Fig. 6b). The MoO_2/Mo_2C@NC-modified separator

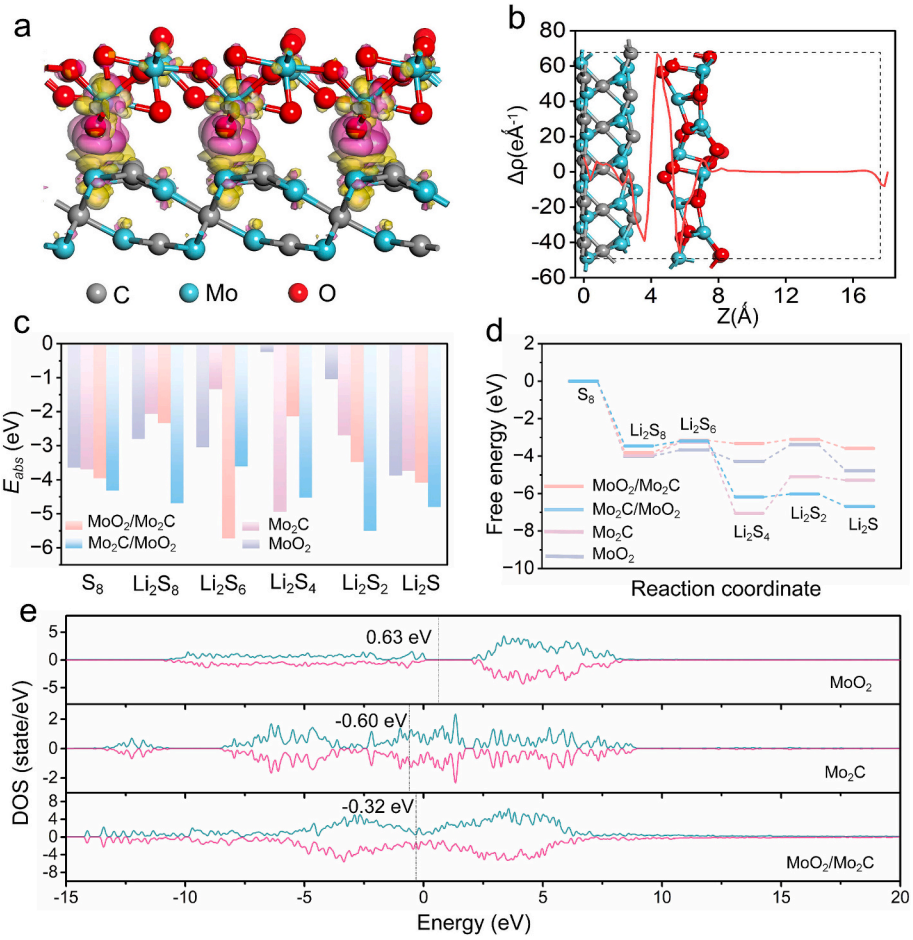

Fig. 5. (a) Difference charge density of the MoO_2/Mo_2C heterostructure; (b) Statistical results along the Z-axis; (c) Adsorption energy of LiPSs on the surface of MoO_2/MoC_2, Mo_2C/MoO_2, Mo_2C, and MoO_2; (d) Gibbs free energy spectrum of S_8 reduced to LiPSs in several electrocatalysts; (e) The comparison of partial density of states (PDOS) and d-band centers for several electrocatalysts.

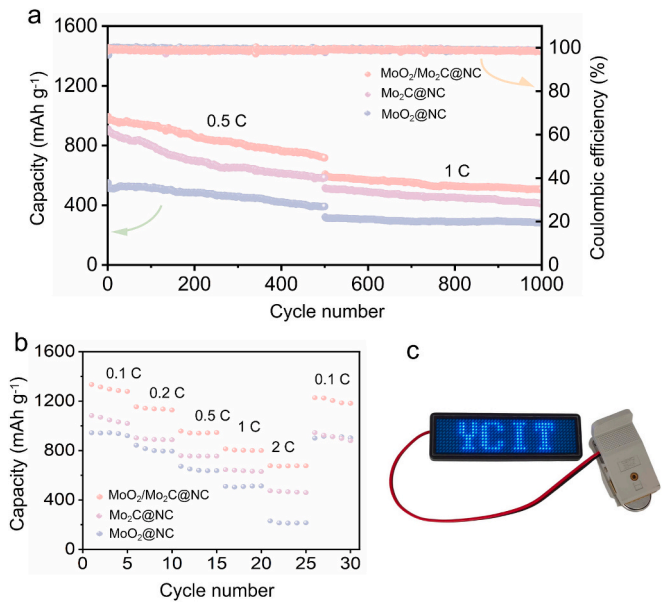

Fig. 6. (a) Li—S batteries employing PP separators modified with MoO_2/Mo_2C@NC, Mo_2C@NC, and MoO_2@NC were tested for long-term cycling stability: 500 cycles at 0.5C and another 500 cycles at 1.0C.; (b) Rate performance; (c) Li—S battery lights up a pattern composed of LED lamps.

delivers a discharge capacity exceeding 1200 mAh g^{-1} at 0.1C, retains ~670 mAh g^{-1} at a high rate of 2C, and recovers to ~1100 mAh g^{-1} when the current density is restored to 0.1C, indicating excellent structural reversibility and rate performance. In comparison, Mo_2C@NC and MoO_2@NC-modified separators exhibit much lower capacities at high rates (467 and 212 mAh g^{-1} at 2C, respectively), consistent with their higher charge transfer impedances. A Li—S battery with the MoO_2/Mo_2C@NC-modified separator was successfully used to power an LED array displaying "YCIT" (Fig. 6c), verifying the practical application potential of the material for real-world energy storage systems.

4. Conclusion

In summary, this work develops a rational and facile strategy for in-situ constructing MoO_2/Mo_2C heterojunctions on N-doped carbon microspheres (MoO_2/Mo_2C@NC) by simply adjusting the mass ratio of dopamine hydrochloride to molybdate precursor. The as-prepared composite acts as a highly efficient polysulfide-regulating interlayer for Li—S batteries, and the significant work-function difference between MoO_2 and Mo_2C induces a strong built-in electric field at the heterointerface, which drives directional electron transfer from Mo_2C to MoO_2. This unique electronic structure synergistically integrates robust LiPS chemisorption on polar MoO_2 and fast catalytic conversion on conductive Mo_2C, which optimizes the LiPS conversion pathway and lowers the reaction energy barrier, realizing a short-path "adsorption-conversion" synergy. The N-doped carbon matrix not only improves the dispersion of MoO_2/Mo_2C heterostructures but also optimizes electron/ion transport in the interlayer. When applied as a coating on commercial PP separators, the MoO_2/Mo_2C@NC composite enhanced the electrochemical performance of Li—S batteries remarkably: the battery delivered a reversible capacity of over 1200 mAh g^{-1} at 0.1C, retained 670 mAh g^{-1} at a high rate of 2C, and maintained ~515 mAh g^{-1} after 1000 cycles. This study not only provides a facile and controllable synthesis strategy for metal oxide/carbide heterostructures but also elucidates the intrinsic synergistic mechanism of polar oxide-conductive carbide heterointerfaces in regulating LiPS behavior. The findings offer a novel design principle for multifunctional electrocatalytic materials toward high-energy-density sulfur-based batteries.

CRediT authorship contribution statement

Lin Sun: Writing – review & editing, Writing – original draft, Project administration, Funding acquisition, Formal analysis, Data curation, Conceptualization. **Tianqi Wang:** Methodology, Investigation, Data curation. **Jie Xie:** Writing – review & editing, Visualization, Data curation. **Yunjing Qiao:** Investigation, Data curation. **Xuetao Lu:** Data curation. **Menghan Liu:** Data curation. **Cheng Liu:** Writing – review & editing, Supervision, Software, Resources. **Zhong Jin:** Writing – review & editing, Supervision, Funding acquisition.

Declaration of competing interest

The authors declare that they have no known competing financial interests or personal relationships that could have appeared to influence the work reported in this paper.

Acknowledgments

The authors gratefully acknowledge financial support from National Natural Science Foundation of China (52202309, U25A20628, 22561160129, 22479074, 22475096), Qing Lan Project of Jiangsu Province, Major Project for Basic and Natural Sciences Research of Jiangsu Provincial Colleges and Universities (25KJA150006), Science and Technology Cooperation Project with Hong Kong, Macao and Taiwan under the Yancheng City Science and Technology Plan (Ycgh2025008), Postgraduate Scientific Research Innovation Program of Jiangsu Province (KYCX25_3879), the Equipment Pre-Research and Ministry of Education Joint Fund (8091B02052407), the Fundamental Research Program Key Project of Jiangsu Province (BK20253008), the Natural Science Foundation of Jiangsu Province (BK20240400, BK20241236), the Science and Technology Major Project of Jiangsu Province (BG2024013), the Scientific and Technological Achievements Transformation Special Fund of Jiangsu Province (BA2023037), the Academic Degree and Postgraduate Education Reforming Project of Jiangsu Province (JGKT24_C001), the Key Core Technology Open Competition Project of Suzhou City (SYG2024122), the Open Research Fund of Suzhou Laboratory (SZLAB-1308-2024-TS005), and the Chenzhou National Sustainable Development Agenda Innovation Demonstration Zone Provincial Special Project (2023sfq11).

Appendix A. Supplementary data

Supplementary data to this article can be found online at https://doi.org/10.1016/j.jcis.2026.140391.

Data availability

Data will be made available on request.

References

[1] Z. Zhu, T. Jiang, M. Ali, Y. Meng, Y. Jin, Y. Cui, W. Chen, Rechargeable batteries for grid scale energy storage, Chem. Rev. 122 (2022) 16610–16751.
[2] T.M. Gür, Review of electrical energy storage technologies, materials and systems: challenges and prospects for large-scale grid storage, Energ. Environ. Sci. 11 (2018) 2696–2767.
[3] J.S. Searle, F. Malagreca, B.M.G. Denison, A.J. Kibler, D.A. Walsh, L.R. Johnson, D. B. Amabilino, G.N. Newton, Diketopyrrolopyrroles act as redox mediators in lithium-sulfur batteries, ACS Energy Lett.s 10 (2025) 2839–2844.
[4] X.-Y. Li, M. Zhao, Y.-W. Song, C.-X. Bi, Z. Li, Z.-X. Chen, X.-Q. Zhang, B.-Q. Li, J.-Q. Huang, Polysulfide chemistry in metal–sulfur batteries, Chem. Soc. Rev. 54 (2025) 4822–4873.
[5] J. Xie, F. Cheng, R. Chen, Z. Jin, L. Sun, Promoting overall sulfur redox kinetics for Li-S batteries via interfacial synergy in a NiS-$NiTe_2$ heterostructure-modified separator, J. Mater. Chem. A 12 (2024) 10737–10744.
[6] M.J. Theibault, C. Chandler, I. Dabo, H.D. Abruña, Transition metal dichalcogenides as effective catalysts for high-rate lithium-sulfur batteries, ACS Catal. 13 (2023) 3684–3691.

[7] M. Li, H. Liu, H. Li, D. Luan, Z. Liu, X.W. Lou, Electron-deficient cobalt centers realized by rational p-π conjugation regulation for high-performance Li-S batteries, Angew. Chem. Int. Ed. 64 (2025) e202503174.

[8] W. Hu, H. Liu, F. Zhang, X. Wang, L. Pang, S. Wang, J. Li, Synergistic coordination effect of co@N active sites and multilevel porous carbon confinement engineering for boosting catalytic conversion kinetics of lithium polysulfides in Li-S batteries, Chem. Eng. J. 513 (2025) 163176.

[9] W. Hua, H. Li, Z. Hu, T. You, J. Qie, H. Dong, H. Sun, Y. Li, S. Dai, Q.-H. Yang, K. Chen, Phase engineering of 2D telluride crystals for sulfur catalysis in batteries, Adv. Energy Mater. n/a (2025) 2501963.

[10] F. Li, H. Yuan, Y. Wang, Z. Xue, M. He, J. Wang, F. Wu, M. Huang, Y. Xiang, A. Hu, W. Chen, T. Wu, X. Sun, Tailoring li-accelerated motif enables lithium stabilization and polysulfide conversion for long-cycling Li-S batteries, Adv. Funct. Mater. 35 (2025) e11078.

[11] J. Guo, Q. Yang, Y. Dou, X. Ba, W. Wei, J. Liu, Shelf life of lithium-sulfur batteries under lean electrolytes: status and challenges, Energ. Environ. Sci. 17 (2024) 1695–1724.

[12] D. Jin, M.R. Krumov, R.M. Mandel, P.J. Milner, H.D. Abruña, Prussian blue analogue framework hosts for Li-S batteries, ACS Energy Lett. 9 (2024) 5822–5829.

[13] H. Raza, S. Bai, J. Cheng, S. Majumder, H. Zhu, Q. Liu, G. Zheng, X. Li, G. Chen, Li-S batteries: challenges, achievements and opportunities, Electrochem. Energy Rev. 6 (2023) 29.

[14] C. Zhao, Y. Huang, P. Wang, Z. Chen, Y. Zhang, N. Zhang, Intrinsic stabilization of vacancies in catalysts via high-entropy approach for lithium-sulfur batteries, Natl. Sci. Rev. 12 (2025) nwaf375.

[15] Y. Yu, Q. Xie, X. Li, Z. Yuan, H. Zhang, Y. Wang, Y. Yao, W. Lei, Regulating the electronic modulation configuration of Mn_xFeCoNiCu high entropy alloy for reliable sulfur redox kinetics, Appl. Catal. B Environ. Energy 363 (2025) 124788.

[16] B. Li, P. Wang, J. Yuan, N. Song, J. Feng, S. Xiong, B. Xi, P-doped $RuSe_2$ on porous N-doped carbon matrix as catalysts for accelerated sulfur redox reactions, Angew. Chem. Int. Ed. 63 (2024) e202408906.

[17] L. Bai, Y. Ren, Q. Zheng, J. Nie, B. Du, Modification of polypropylene separator with nickel and manganese oxide-decorated carbon nanotubes toward high-performance lithium-sulfur batteries, J. Power Sources 633 (2025) 236353.

[18] S. Ge, Q. Zhao, Y. Liu, F. Wang, G. Wei, Y. Liu, B. Xu, Ultrathin 2D–2D MXene-LDH interlayer with high polysulfide adsorption ability for advanced Li–S batteries, ACS Appl. Mater. Interfaces 16 (2024) 50650–50658.

[19] Y. Kong, X. Qiu, Y. Xue, G. Li, L. Qi, W. Yang, T. Liu, Y. Li, Sulfonic acid-functionalized graphdiyne for effective Li-S battery separators, J. Am. Chem. Soc. 146 (2024) 23764–23774.

[20] D. Han, L. Sun, Z. Li, W. Qin, L. Zhai, Y. Sun, S. Tang, Y. Fu, Supramolecular channels via crown ether functionalized covalent organic frameworks for boosting polysulfides conversion in Li-S batteries, Energy Storage Mater. 65 (2024) 103143.

[21] L. Sun, Y. Liu, K. Zhang, F. Cheng, R. Jiang, Y. Liu, J. Zhu, Z. Jin, H. Pang, Rapid construction of highly-dispersed cobalt nanoclusters embedded in hollow cubic carbon walls as an effective polysulfide promoter in high-energy lithium-sulfur batteries, Nano Res. 15 (2022) 5105–5113.

[22] Z. Qi, J. Jiang, P. Yao, Z. Lu, Y. Shen, S. Liu, J. Sun, P. Xiong, X. Wang, X. Ouyang, J. Zhu, Y. Fu, Co3O4/C-NFs induced 3D electric field enhancement for dual-regulation of polysulfides and li+ transport in lithium–sulfur batteries, Adv. Sci. n/a (2025) e20167.

[23] N. Song, J. Ma, Y. Liang, P. Wang, J. Yuan, S. Xiong, X. Li, J. Feng, B. Xi, Phase and orbital engineering effectuating efficient adsorption and catalysis toward high-energy lithium-sulfur batteries, Adv. Mater. 37 (2025) 2420588.

[24] K. Chen, Y. Zhu, Z. Huang, B. Han, Q. Xu, X. Fang, J. Xu, Strengthened d-p orbital hybridization on metastable cubic Mo_2C for highly stable lithium-sulfur batteries, ACS Nano 18 (2024) 34791–34802.

[25] B. Wang, J. Tang, S. Jia, Z. Xing, S. Chen, Y. Deng, X. Meng, S. Tang, General scalable synthesis of mesoporous metal oxide nanosheets with high crystallinity for ultralong-life Li-S batteries, Adv. Funct. Mater. 34 (2024) 2315836.

[26] F.-J. Liu, W.-L. Luo, Z. Zhang, J. Yu, J.-X. Cai, Z.-Y. Yang, Cation-doped V_2O_5 microsphere as a bidirectional catalyst to activate sulfur redox reactions for lithium-sulfur batteries, Chem. Eng. J. 456 (2023) 140948.

[27] W. Xia, H. Liu, H. Liu, Q. Liang, L. Yi, M. Chen, X. Wang, X. Wu, H. Shu, Interface-driven d-band modulation for dual-function anchoring and catalytic conversion of polysulfides in lithium-sulfur batteries, J. Energy Chem. 107 (2025) 919–928.

[28] H. Li, C. Chen, Y. Yan, T. Yan, C. Cheng, D. Sun, L. Zhang, Utilizing the built-in electric field of p-n junctions to spatially propel the stepwise polysulfide conversion in lithium-sulfur batteries, Adv. Mater. 33 (2021) 2105067.

[29] D. Lei, W. Shang, X. Zhang, Y. Li, S. Qiao, Y. Zhong, X. Deng, X. Shi, Q. Zhang, C. Hao, X. Song, F. Zhang, Facile synthesis of heterostructured MoS_2–MoO_3 nanosheets with active electrocatalytic sites for high-performance lithium–sulfur batteries, ACS Nano 15 (2021) 20478–20488.

[30] J. Lee, C. Choi, J.B. Park, S. Yu, J. Ha, H. Lee, G. Jang, Y.S. Park, J. Yun, H. Im, S. Moon, S. Lee, J.-I. Choi, D.-W. Kim, J. Moon, Optimally arranged TiO_2@MoS_2 heterostructures with effectively induced built-in electric field for high-performance lithium-sulfur batteries, J. Energy Chem. 83 (2023) 496–508.

[31] X.A.-O. Liu, J. Wang, W. Wang, Y. Liu, J. Sun, H. Wang, Q. Zhao, W. Liu, Q. Huang, S. Wang, Q. An, Q. Wang, L. Shen, J.A.-O. Wang, Interfacial synergy in Mo_2C/MoC heterostructure promoting sequential polysulfide conversion in high-performance lithium-sulfur battery, Small 20 (12) (2024) 2307902.

[32] M. Jia, H. Jiang, J. Jia, J. Sun, L. Hou, J. Deng, C. Yuan, Endogenous MoC/Mo_2C nanoscale heterostructures confined in hollow porous carbon spheres toward sodium-ion capacitors, Adv. Energy Mater. 15 (2025) e03529.

[33] H. Liu, X. Tian, Y. Liu, H.A. Munir, W. Hu, X. Fan, X. Liu, L. Pang, Synergistic polysulfides adsorption–conversion with Mo_2C-MoO_2 heterostructure for kinetically enhanced lithium–sulfur battery, Energ. Technol. 12 (2024) 2300820.

[34] Y. He, Y. Luo, W. Zhang, S. Liu, K. Zhu, L. Huang, Y. Yang, X. Li, R. Yu, H. Shu, X. Wang, M. Chen, MoO2/t-C3N4 heterogeneous materials with bidirectional catalysis for the rapid conversion of s species in Li-S batteries, ACS Appl. Mater. Interfaces 15 (2023) 45915–45925.

[35] X.-L. Wang, L. Sun, L. Yang, J. Zhao, Q. Xu, Hybrid zeolitic imidazolate framework-derived Co_3Mo/Mo_2C heterostructure for enhanced oxygen evolution reaction, Adv. Funct. Mater. 34 (2024) 2314247.

[36] Y.T. Baheri, M.A. Hedayati, M. Maleki, H. Karimian, A. Shokrieh, M.M. Shokrieh, A. Imani, Y. Tong, In-situ synthesis of MoO_2/MoS_2 nanoparticles embedded in nitrogen-doped carbon foam as an anode for ultra long-life lithium-ion battery, J. Power Sources 645 (2025) 237099.

[37] Y. Gao, S. Zhang, L. Xu, X. Li, L. Li, L. Bao, J. Peng, X. Li, Fast charge transport motivated by tunable Mo_2C/Mo_2N high-quality heterointerface for superior pseudocapacitive storage, J. Energy Chem. 83 (2023) 465–477.

[38] Y. Zhang, S. Guo, X. Xin, Y. Song, L. Yang, B. Wang, L. Tan, X. Li, Plasmonic MoO_2 as co-catalyst of MoS_2 for enhanced photocatalytic hydrogen evolution, Appl. Surf. Sci. 504 (2020) 144291.

[39] Y. Huang, X. Li, P.K. Shen, C. Yang, J. Zhu, High-performance MoP-Mo_2C/C heterogeneous nanoparticle catalysts for alkaline hydrogen evolution and oxidation reactions, ACS Mater. Lett. 6 (2024) 1678–1685.

[40] A. Huang, Y. Wu, H. Huang, C. Li, Y. Sun, L. Li, S. Peng, Lithiophilic Mo_2C clusters-embedded carbon nanofibers for high energy density lithium metal batteries, Adv. Funct. Mater. 33 (2023) 2303111.

[41] Y. Li, L. Wang, F. Zhang, W. Zhang, G. Shao, P. Zhang, Detecting and quantifying wavelength-dependent electrons transfer in heterostructure catalyst via in situ irradiation XPS, Adv. Sci. 10 (2023) 2205020.

[42] C. Zhao, L. Tian, Z. Zou, Z. Chen, H. Tang, Q. Liu, Z. Lin, X. Yang, Revealing and accelerating interfacial charge carrier dynamics in z-scheme heterojunctions for highly efficient photocatalytic oxygen evolution, Appl. Catal. B Environ. Energy 268 (2020) 118445.

[43] T.-F. Li, J. Li, L.-P. Zhang, J.-W. Ke, M.-X. Fan, L.-F. Zhang, C.-W. Deng, Y. Sun, T. Qian, C.-L. Yan, Work-function-induced interfacial electron redistribution of MoO_2/WO_2 heterostructures for high-efficiency electrocatalytic hydrogen evolution reaction, Rare Metals 43 (2024) 489–499.

[44] Q. Wang, J. He, B. Sun, Y. Bai, Y. Yan, J. Xue, Z. Sun, X. Wang, J. Wu, J. Wang, R. Zhao, Z. Sun, H.K. Liu, S.X. Dou, Recent advances and strategies of metal sulfides for accelerating polysulfide redox and regulating li plating, ACS Nano 19 (2025) 28992–29027.

[45] S. Deng, T. Guo, J. Heier, C. Zhang, Unraveling polysulfide's adsorption and electrocatalytic conversion on metal oxides for Li-S batteries, Adv. Sci. 10 (2023) 2204930.

[46] R. Liu, Z. Huang, J. Li, M. Liu, Y. Xu, C. Li, F. Dai, X. Wang, T. Mei, Structurally mutualized Ti3C2@Ni2P catalysts realize interfacial charge redistribution for facilitating redox reaction kinetics in lithium–sulfur batteries, ACS Appl. Mater. Interfaces 17 (2025) 28267–28275.

[47] Z. Liu, M. Chen, D. Zhou, Z. Xiao, Scavenging of “dead sulfur” and “dead lithium” revealed by integrated–heterogeneous catalysis for advanced lithium–sulfur batteries, Adv. Funct. Mater. 33 (2023) 2306321.

[48] L. Sun, H. Xu, J. Xie, Y. Yuan, H. Wang, M. Wang, X. Chen, Z. Jin, D-band center modulation of metallic co-incorporated Co7Fe3 alloy heterostructure for regulating polysulfides in highly efficient lithium-sulfur batteries, Adv. Funct. Mater. 35 (2025) 2416826.